

RESEARCH ARTICLE

10.1002/2014JE004653

Key Point:

- Scaling laws are derived from numerical models in 3-D spherical geometry

Correspondence to:

C. Yao,
chloe.yao@erdw.ethz.ch

Citation:

Yao, C., F. Deschamps, J. P. Lowman, C. Sanchez-Valle, and P. J. Tackley (2014), Stagnant lid convection in bottom-heated thin 3-D spherical shells: Influence of curvature and implications for dwarf planets and icy moons, *J. Geophys. Res. Planets*, 119, 1895–1913, doi:10.1002/2014JE004653.

Received 24 APR 2014

Accepted 29 JUL 2014

Accepted article online 3 AUG 2014

Published online 15 AUG 2014

Stagnant lid convection in bottom-heated thin 3-D spherical shells: Influence of curvature and implications for dwarf planets and icy moons

C. Yao¹, F. Deschamps², J. P. Lowman³, C. Sanchez-Valle¹, and P. J. Tackley¹

¹Department of Earth Sciences, Swiss Federal Institute of Technology Zurich, Zurich, Switzerland, ²Institute of Earth Sciences, Academia Sinica, Taipei, Taiwan, ³Department of Physical and Environmental Sciences, University of Toronto, Scarborough, Toronto, Ontario, Canada

Abstract Because the viscosity of ice is strongly temperature dependent, convection in the ice layers of icy moons and dwarf planets likely operates in the stagnant lid regime, in which a rigid lid forms at the top of the fluid and reduces the heat transfer. A detailed modeling of the thermal history and radial structure of icy moons and dwarf planets thus requires an accurate description of stagnant lid convection. We performed numerical experiments of stagnant lid convection in 3-D spherical geometries for various ice shell curvatures f (measured as the ratio between the inner and outer radii), effective Rayleigh number Ra_m , and viscosity contrast $\Delta\eta$. From our results, we derived scaling laws for the average temperature of the well-mixed interior, θ_m , and the heat flux transported through the shell. The nondimensional temperature difference across the bottom thermal boundary layer is well described by $(1 - \theta_m) = \frac{1.23}{\gamma f^{1.5}}$, where γ is a parameter that controls the magnitude of the viscosity contrast. The nondimensional heat flux at the bottom of the shell, F_{bot} , scales as $F_{bot} = \frac{1.46 Ra_m^{0.27}}{\gamma^{1.21} f^{1.78}}$. Our models also show that the development of the stagnant lid regime depends on f . For given values of Ra_m and $\Delta\eta$, the stagnant lid is less developed as the shell's curvature increases (i.e., as f decreases), leading to improved heat transfer. Therefore, as the outer ice shells of icy moons and dwarf planets grow, the effects of a stagnant lid are less pronounced.

1. Introduction

The cooling of icy satellites is controlled by the heat transfer through their outer ice layer [Hussmann *et al.*, 2007]. The physical (thickness and thermal conductivity) and rheological (viscosity) properties of this layer allow thermal convection to operate within it and thus to enhance heat transport from the satellite's interior toward its surface. The convective flow and the efficiency of the heat transfer may, however, be influenced by several parameters such as the rheology of the fluid, the geometry of the system, and the mode of heating. For a plane layer isoviscous fluid heated from below, the top and bottom thermal boundary layers (TBLs) are symmetric. This symmetry can be broken by several parameters, including viscosity variations throughout the fluid (for instance, due to temperature variations) [Christensen, 1984; Solomatov, 1995], spherical geometry [Shahnas *et al.*, 2008; Deschamps *et al.*, 2010], and the addition of internal heating [Travis and Olson, 1994; Sotin and Labrosse, 1999]. Because thermal convection is fundamentally controlled by the growth of instabilities in TBLs [Howard, 1966], the flow and efficiency of heat transfer are strongly affected by this symmetry breaking.

The viscosity of ice is strongly temperature dependent. In this case, convection occurs in the stagnant lid regime: a rigid, thermally conductive lid forms at the top of the fluid, and convection is restricted to the layer located between the bottom of the lid and the bottom of the system (hereafter referred to as the convective layer) [Davaille and Jaupart, 1993; Grasset and Parmentier, 1998; Solomatov, 1995; Moresi and Solomatov, 1995]. The presence of the lid considerably reduces the heat transfer to the surface and increases the average temperature in the convective layer with respect to the isoviscous case. The increase in average temperature implies that the temperature jump in the bottom TBL is reduced. The lid accommodates most of the viscosity jump, and the viscosity jump across the sublayer is about a factor of 10 [Davaille and Jaupart, 1993]. Therefore, this convective layer is often considered to be nearly isoviscous [Solomatov, 1995].

The heat transfer may also depend on the geometry. Numerical experiments [Shahnas *et al.*, 2008; Deschamps *et al.*, 2010] have reported important changes in the flow pattern and in the average properties

of the fluid in a spherical shell, compared to that in 3-D Cartesian geometry [O'Farrell and Lowman, 2010; O'Farrell et al., 2013]. For an isoviscous layer heated from below, and a given Rayleigh number, the number of plumes generated at the bottom of the shell decreases with decreasing core radius relative to convecting layer thickness (i.e., curvature). Furthermore, average temperature decreases with increasing curvature, and the temperature jump in the bottom TBL is larger than that in the top TBL. This effect is opposite to that induced by temperature-dependent viscosity. Curvature may therefore influence the appearance of the stagnant lid regime.

Ratcliff et al. [1995, 1996] performed numerical experiments in spherical shells with moderate (up to 1000) thermal viscosity contrast. For small viscosity contrast (30 and less) and small enough Rayleigh number, they observed steady patterns (e.g., tetrahedral or cubic patterns). For larger viscosity contrasts, the flow is time dependent, and more complex structures are observed. In all cases, however, the interior temperature increases with increasing viscosity contrast. Note that the viscosity contrasts imposed in these experiments are too small for convection to operate in the stagnant lid regime. Reese et al. [1999, 2005] conducted experiments for a purely volumetrically heated fluid with viscosity contrast up to 2.0×10^6 , i.e., well into the stagnant lid regime and found that the flow is dominated by cylindrical upwellings surrounded by downwelling sheets. Their results further suggest that the heat flux can be modeled with scaling laws similar to those found in 2-D Cartesian geometry for internally heated fluids. For a shell heated from below, Yoshida and Kageyama [2004] observed that convection operates in different regimes, depending on the viscosity contrast. The flow is also dominated by an irregular network of cylindrical plumes surrounded by cold downwellings, the number of plumes depending on the viscosity contrast, and the Rayleigh number. In all these studies, however, the ratio between the inner and outer radii of the shell was fixed to 0.55. This curvature is well suited for the Earth's mantle but not for the outer ice shell of icy moons.

In the present study, we performed a series of stagnant lid thermal convection experiments in 3-D spherical shells in order to explore the influence of the Rayleigh number, thermal viscosity contrast, and curvature of the shell. We then use the results of these experiments to build scaling laws for the average temperature of the shell and for the surface heat flux as a function of the explored parameters. Additionally, we present experiments for a few cases that did not reach the stagnant lid regime to constrain the limits of this regime.

2. Physical Model

We performed numerical experiments of thermal convection using StagYY [Tackley, 2008], which solves the conservation equations of mass, energy and momentum for an incompressible, infinite Prandtl number fluid in 3-D spherical geometry. Spherical shells are modeled with Yin-Yang grids. The curvature of the shell is controlled by the ratio f of the core-to-total radius,

$$f = \frac{R_c}{(R_c + D)}, \quad (1)$$

where R_c is the radius of the core and D is the thickness of the modeled layer. The layer thus becomes thinner relative to the core radius with increasing f , and small values of f are associated with high degrees of curvature. Note that f varies from 0 for a sphere (the system has no core) to 1 for an infinite slab (3-D Cartesian case). Here we performed experiments for values of f ranging between 0.3 and 0.92. The system is heated from below and cooled at the top. The boundaries at R_c and $R_c + D$ are both free slip and isothermal.

The viscosity η varies with the temperature T according to the Frank-Kamenetskii approximation of an Arrhenius law

$$\eta(T) = \eta_0 \exp \left[-\gamma \frac{(T - T_0)}{\Delta T} \right], \quad (2)$$

where η_0 and T_0 are the viscosity and temperature values at the surface, ΔT is the superadiabatic temperature difference between the bottom and the top of the fluid, and γ is a parameter that controls the magnitude of the viscosity contrast. Note that the nomenclature is different from that of Solomatov [1995] but stays consistent with previous similar studies [Grasset and Parmentier, 1998; Deschamps and Lin, 2014]. For clarity, we list the correspondance between the two nomenclatures in Table 1.

Table 1. Nomenclature Used in This Study^a

Symbol	Description	Solomatov [1995]
α	thermal expansion coefficient	
γ	viscosity coefficient	p
D	thickness of layer	d
d_{lid}	nondimensional thickness of the stagnant lid	
E_a	activation energy	E
η	viscosity	
η_{ref}	reference viscosity	
f	curvature parameter	
f_{CL}	ratio between the core radius and the radius at the base of the stagnant lid	
F	nondimensional heat flux	
\bar{F}	time-averaged conductive heat flux	
Φ_{cond}	dimensional conductive heat flux in spherical geometry	
Φ	dimensional heat flux	F
g	gravitational acceleration	
k	thermal conductivity	
κ	thermal diffusivity	
Nu	average Nusselt number	
\mathcal{R}	gas constant	
R	total radius	
R_c	core radius	
Ra	Rayleigh number	
$Ra_{1/2}$	median Rayleigh number	
Ra_0	surface Rayleigh number	
Ra_{bot}	bottom Rayleigh number	
Ra_m	effective Rayleigh number	Ra_i
ρ	reference density	
t	time	
T_0	dimensional surface temperature	
$T_{1/2}$	median temperature	
T_{bot}	bottom temperature	
T_m	temperature of the well-mixed interior	
T_{ref}	reference temperature	
ΔT	dimensional temperature difference between the surface and the bottom	
ΔT_c	dimensional temperature jump across the conductive domain	
ΔT_v	viscous temperature scale	
δT_0	nondimensional temperature jump across the layer formed by the stagnant lid and the top TBL	
δT_{bot}	nondimensional temperature jump across the bottom TBL	
θ_m	nondimensional temperature of the well-mixed interior	T_i
θ_{lid}	nondimensional temperature at the bottom of the stagnant lid	
θ_{CL}	nondimensional temperature of the well-mixed interior rescaled to the convective layer	

^aA correspondance with Solomatov [1995] nomenclature is shown, if different. Note that nondimensional temperatures are expressed by θ and dimensional temperatures by T .

The viscosity contrast is defined by the ratio between the highest and the lowest viscosity (which are located at the outer and inner radii of the shell, respectively)

$$\Delta\eta = \frac{\eta(T_0)}{\eta(T_0 + \Delta T)} = \exp(\gamma). \quad (3)$$

The vigor of convection is controlled by the Rayleigh number

$$Ra = \frac{\alpha \rho g \Delta T D^3}{\eta \kappa}, \quad (4)$$

where α , ρ , and κ are the fluid's thermal expansion coefficient, reference density, and thermal diffusivity, g is the acceleration due to gravity, and D is the thickness of the layer. Because viscosity depends on temperature, the definition of the Rayleigh number is not unique. We define a reference Rayleigh number Ra_0 calculated at the surface temperature T_0 , which is common to all calculations. Other definitions of reference

Rayleigh number often used are the median Rayleigh number $Ra_{1/2}$ calculated from the median temperature $T_{1/2} = T_0 + \Delta T/2$ and the bottom Rayleigh number Ra_{bot} calculated at temperature $T_{\text{bot}} = T_0 + \Delta T$. Following our viscosity law (equation (2)), these Rayleigh numbers are related to the surface Rayleigh number by

$$Ra_{1/2} = Ra_0 \exp(\gamma/2) \quad (5)$$

$$Ra_{\text{bot}} = Ra_0 \exp(\gamma) \quad (6)$$

It is also useful to define a Rayleigh number for the well-mixed interior, Ra_m (hereafter referred to as the effective Rayleigh number), calculated with the average temperature T_m of the well-mixed interior. This effective Rayleigh number takes into account the effect of viscosity variations. In our experiments, we prescribe the surface Rayleigh number Ra_0 and calculate the effective Rayleigh number Ra_m with

$$Ra_m = Ra_0 \exp(\gamma\theta_m), \quad (7)$$

where $\theta_m = (T_m - T_0)/\Delta T$ is the nondimensional temperature of the well-mixed interior. The temperature θ_m is computed from the isothermal part of the horizontally averaged profile of temperature of the layer. Another important parameter is the Nusselt number Nu , measuring the efficiency of the convective heat transfer compared to the conductive heat transfer. Nu is defined by the ratio of the laterally averaged heat flux normalized by the conductive heat flux Φ_{cond} found in the absence of convection. This varies with the radius r , such that

$$\Phi_{\text{cond}} = \frac{f}{(1-f)^2} k \Delta T \frac{D}{r^2}, \quad (8)$$

where k is the thermal conductivity.

With this characteristic heat flux, energy conservation implies that Nu is constant throughout the shell thickness. Alternatively, heat flux may be nondimensionalized with the Cartesian conductive heat flux, $k\Delta T/D$. With this definition, the conservation of energy requires that the surface and bottom nondimensional heat flux, F_{top} and F_{bot} , satisfy

$$F_{\text{top}} = f^2 F_{\text{bot}}. \quad (9)$$

Dividing the laterally averaged heat flux by the conductive heat flux Φ_{cond} with $r = R_c$ at the bottom of the shell, and $r = R_c + D = R$ at its top, the Nusselt number at the top and at the bottom become

$$Nu_{\text{top}} = F_{\text{top}} \frac{(1-f)^2}{f} \frac{R^2}{D^2}, \quad (10)$$

$$Nu_{\text{bot}} = F_{\text{bot}} \frac{(1-f)^2}{f} \frac{R_c^2}{D^2},$$

where R is the total radius. Noting that $R/D = 1/(1-f)$ and $R_c/D = f/(1-f)$, equation (10) leads to

$$Nu_{\text{top}} = \frac{F_{\text{top}}}{f}, \quad (11)$$

$$Nu_{\text{bot}} = F_{\text{bot}} f.$$

Using equation (9), one can easily check that $Nu_{\text{top}} = Nu_{\text{bot}}$.

The grid resolution for each of the two Yin-Yang blocks, $npx \times npy \times npz$, is adjusted according to the curvature and the effective Rayleigh number. For effective Rayleigh number lower than 10^7 and f lower than 0.9, we use a grid resolution of $128 \times 384 \times 64$. For higher values of f , we increase the lateral grid size to 256×768 to properly resolve the large number of small plumes generated for such curvatures. For higher effective Rayleigh number, we increase the vertical resolution to 128 points in order to better resolve the thermal boundary layers. The initial condition for the temperature consists of an adiabatic profile with thin superadiabatic boundary layers at the top and bottom of the shell, to which small random perturbations are added. Calculations are carried on until a quasi-stationary state is reached, i.e., when the average temperature $\langle T \rangle$ and the nondimensional heat flux oscillate around constant values. For each calculation, we determine these values by averaging over several oscillations. An additional criterion of convergence is to check that the conservation of energy is verified (equation (9)).

Table 2. Thermal Convection Experiments in 3-D Spherical Geometry^a

f	Ra_0	$\Delta\eta$	Grid Size	θ_m	F_{top}	F_{bot}	Nu	d_{lid}	Ra_m	Regime
0.3	31.62	1.00×10^5	128*384*64	0.2510	0.458	5.082	1.526	-	5.69×10^2	Marginally critical
0.3	17.68	3.20×10^5	128*384*64	0.2593	0.427	4.757	1.4245	-	4.73×10^2	Marginally critical
0.3	10.00	1.00×10^6	128*384*64	0.2664	0.408	4.459	1.3485	-	3.97×10^2	Marginally critical
0.3	5.59	3.20×10^6	128*384*64	0.2676	0.395	4.407	1.3195	-	3.08×10^2	Marginally critical
0.3	320.00	1.00×10^4	128*384*64	0.1817	0.825	9.203	2.7563	-	1.71×10^3	Weak
0.3	32.00	1.00×10^6	128*384*64	0.2829	0.638	7.053	2.127	-	1.59×10^3	Marginally critical
0.3	100.00	1.00×10^6	128*384*64	0.2727	0.942	10.364	3.141	-	4.33×10^3	Weak
0.4	100.00	1.00×10^4	128*384*64	0.2725	0.760	4.734	1.897	-	1.23×10^3	Weak
0.4	55.90	3.20×10^4	128*384*64	0.3452	0.815	5.090	2.037	-	2.01×10^3	Weak
0.4	31.62	1.00×10^5	128*384*64	0.3722	0.795	4.965	1.987	-	2.30×10^3	Weak
0.4	17.68	3.20×10^5	128*384*64	0.3954	0.783	4.896	1.958	-	2.66×10^3	Weak
0.4	10.00	1.00×10^6	128*384*64	0.4240	0.799	5.001	2.000	-	3.50×10^3	Weak
0.4	101.19	1.00×10^5	256*768*128	0.3850	1.241	7.773	3.107	-	8.51×10^3	Weak
0.5	100.00	1.00×10^4	128*384*64	0.3761	1.122	4.497	2.247	-	3.19×10^3	Weak
0.5	55.90	3.20×10^4	128*384*64	0.4672	1.203	4.813	2.407	-	7.12×10^3	Weak
0.5	31.62	1.00×10^5	128*384*64	0.5477	1.290	5.157	2.580	-	1.73×10^4	Weak
0.5	17.68	3.20×10^5	128*384*64	0.7312	1.599	6.400	3.199	0.325	1.87×10^5	Stagnant lid
0.5	10.00	1.00×10^6	256*768*128	0.7550	1.711	6.844	3.423	0.315	3.39×10^5	Stagnant lid
0.5	101.19	1.00×10^5	256*768*128	0.6800	2.166	8.649	4.329	0.217	2.54×10^5	Stagnant lid
0.6	55.90	3.20×10^4	128*384*64	0.7142	1.845	5.124	3.075	0.289	9.23×10^4	Stagnant lid
0.6	31.62	1.00×10^5	128*384*64	0.7596	1.925	5.341	3.207	0.295	1.99×10^5	Stagnant lid
0.6	17.68	3.20×10^5	128*384*64	0.7911	1.982	5.502	3.302	0.296	4.00×10^5	Stagnant lid
0.6	10.00	1.00×10^6	128*384*64	0.8120	2.098	5.829	3.497	0.292	7.45×10^5	Stagnant lid
0.7	55.90	3.20×10^4	128*384*64	0.7760	2.194	4.484	3.137	0.275	1.75×10^5	Stagnant lid
0.7	31.62	1.00×10^5	128*384*64	0.8122	2.241	4.579	3.204	0.284	3.64×10^5	Stagnant lid
0.7	17.68	3.20×10^5	128*384*64	0.8360	2.363	4.824	3.376	0.281	7.08×10^5	Stagnant lid
0.7	10.00	1.00×10^6	128*384*64	0.8535	2.505	5.117	3.581	0.274	1.32×10^6	Stagnant lid
0.7	20.00	1.00×10^6	128*384*64	0.8502	3.067	6.261	4.382	0.225	2.53×10^6	Stagnant lid
0.8	100.00	1.00×10^4	128*384*64	0.7941	2.469	3.841	3.08	0.260	1.50×10^5	Stagnant lid
0.8	55.90	3.20×10^4	128*384*64	0.8254	2.498	3.895	3.119	0.269	2.92×10^5	Stagnant lid
0.8	31.62	1.00×10^5	128*384*64	0.8512	2.587	4.035	3.231	0.265	5.70×10^5	Stagnant lid
0.8	17.68	3.20×10^5	128*384*64	0.8692	2.714	4.236	3.390	0.267	1.08×10^6	Stagnant lid
0.8	14.00	1.00×10^6	192*576*128	0.8794	3.18	4.972	3.976	0.238	2.65×10^6	Stagnant lid
0.8	10.00	1.00×10^6	256*768*64	0.8793	2.871	4.485	3.588	0.258	1.89×10^6	Stagnant lid
0.8	101.19	1.00×10^5	256*768*64	0.8520	3.636	5.681	4.545	0.198	1.84×10^6	Stagnant lid
0.8	32.00	1.00×10^6	256*768*64	0.8740	3.941	6.158	4.926	0.191	5.62×10^6	Stagnant lid
0.8	5.60	1.00×10^8	192*576*128	0.8919	6.372	9.965	7.965	0.121	7.65×10^7	Stagnant lid
0.8	316.23	1.00×10^5	192*576*128	0.8496	5.003	7.824	6.256	0.148	5.60×10^6	Stagnant lid
0.8	176.78	3.20×10^5	192*576*128	0.8637	5.186	8.100	6.480	0.148	1.01×10^7	Stagnant lid
0.867	100.00	1.00×10^4	128*384*64	0.8256	2.634	3.495	3.035	0.258	2.01×10^5	Stagnant lid
0.867	101.19	1.00×10^5	128*384*64	0.8676	4.031	5.367	4.651	0.182	2.20×10^6	Stagnant lid
0.9	100.00	1.00×10^4	256*768*64	0.8305	2.726	3.359	3.026	0.254	2.10×10^5	Stagnant lid
0.9	55.90	3.20×10^4	256*768*64	0.8585	2.773	3.424	3.081	0.262	4.12×10^5	Stagnant lid
0.9	31.62	1.00×10^5	256*768*64	0.8763	2.866	3.540	3.186	0.262	7.61×10^5	Stagnant lid
0.9	17.68	3.20×10^5	256*768*64	0.8886	3.054	3.768	3.393	0.253	1.38×10^6	Stagnant lid
0.9	10.00	1.00×10^6	256*768*64	0.8980	3.217	3.972	3.574	0.244	2.44×10^6	Stagnant lid
0.92	100.00	1.00×10^4	256*768*64	0.8369	2.762	3.263	3.002	0.254	2.23×10^5	Stagnant lid
0.92	101.19	1.00×10^5	256*768*64	0.8719	4.151	4.905	4.513	0.183	2.32×10^6	Stagnant lid

^aThe temperature of the well-mixed interior, θ_m , depends on the convective regime: it represents the temperature of the well-mixed interior, when such regions exist (stagnant lid regime), or the middepth temperature in other cases (marginally critical and weak regimes).

3. Flow Pattern and Time Variations

We conducted a series of experiments featuring stagnant lid thermal convection in 3-D spherical shells heated from below, with values of f in the range 0.3–0.92, viscosity contrasts varying between 10^4 and 10^8 , and surface Rayleigh numbers from 5 to 300. The results are listed in Table 2.

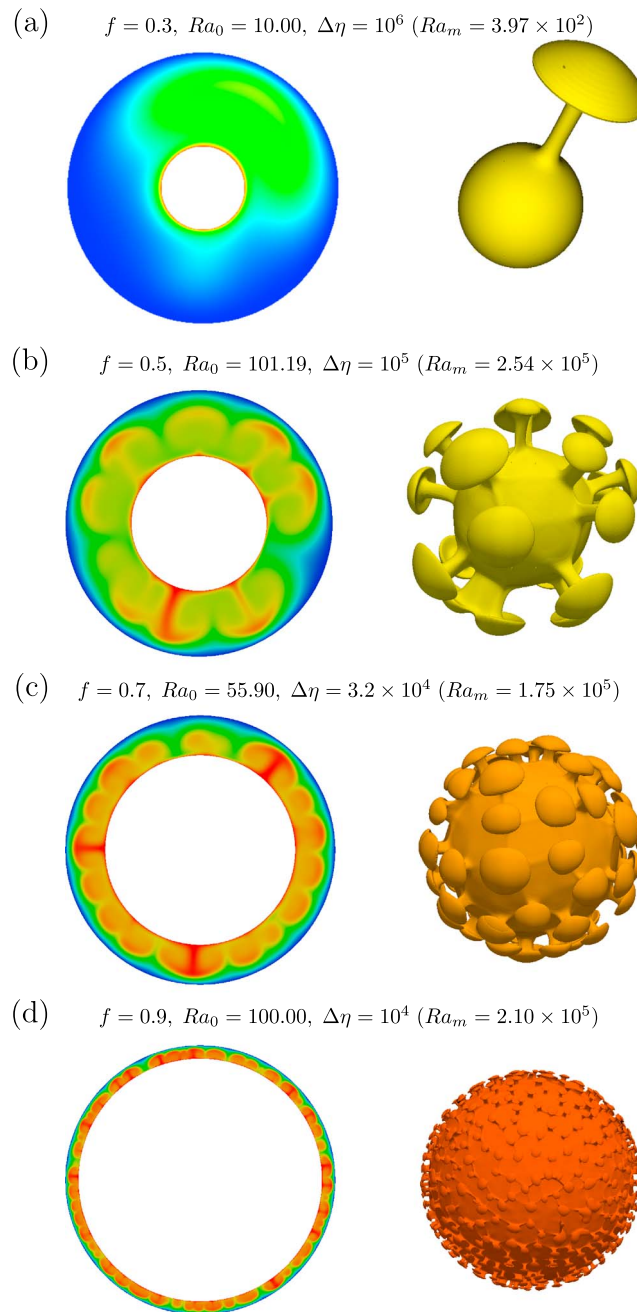


Figure 1. Isosurface and slice of temperature for four selected cases with various curvatures.

Ra_m and $\Delta\eta$, as well as the difference between the basal and surface characteristics, may be explained by the time required for instabilities to grow in the top and bottom boundary layers. When the quasi-stationary state is reached, the time-averaged conductive heat flux is equal to heat flux predicted by the half-space cooling model,

$$\bar{F} = \frac{2k\Delta T_c}{\sqrt{\pi\kappa t_c}}, \quad (12)$$

where k is the thermal conductivity, ΔT_c the temperature jump across the conductive domain (either the bottom TBL or the top TBL plus stagnant lid), κ the thermal diffusivity, and t_c the time for the growth of instabilities. Using the diffusion time D^2/κ as the characteristic time and the total temperature jump ΔT as

Figure 1 shows temperature isosurfaces and polar slices for selected cases with different curvature. For cases in the stagnant lid regime (corresponding to $f \geq 0.5$), the convective flow is confined in the layer below the conductive lid. It consists of hot upwelling plumes surrounded by interconnected downwelling sheets. The number of plumes depends on the curvature of the shell, the viscosity contrast, and the Rayleigh number. All cases presented here are time dependent, reaching a quasi-stationary state at the end of the calculation. The mean values for temperature and heat flux are temporal averages determined once the model has reached a quasi-stationary state. The distribution of plumes thus varies with time, but the overall pattern remains unchanged. Oscillation of the average temperature and the nondimensional heat flux around constant values (Figure 2) are associated with these variations.

Figure 2 shows that the amplitude and the frequency of the heat flux oscillations increase with increasing effective Rayleigh number, Ra_m , and for a similar Rayleigh number, the amplitude and frequency increases with decreasing viscosity contrast (Figures 2c and 2d). For all cases, the time averaged heat flux at the top and at the bottom of the system are equal, as required by conservation of energy. However, the details of the oscillations are significantly different. The amplitude of the oscillations at the base is slightly higher than those at the surface of the fluid. More noticeably, the frequency of the oscillations at the surface is much lower than at the base. The dependence of the oscillation frequency on

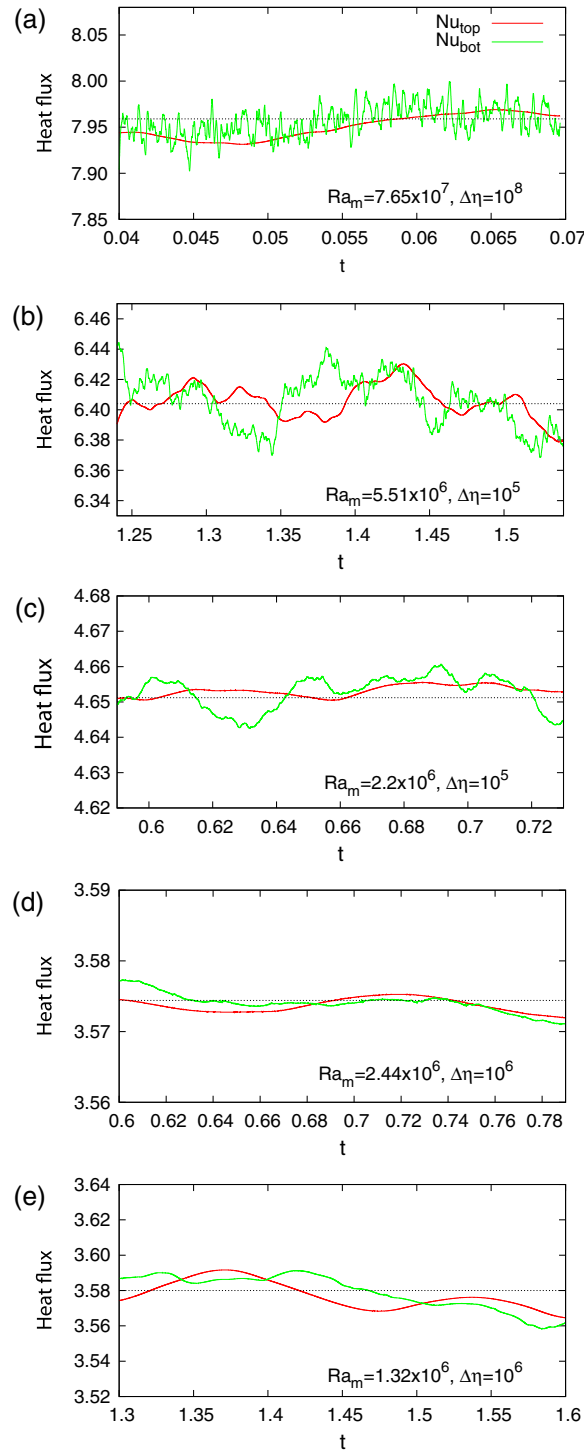


Figure 2. Time evolution of the nondimensional surface and basal heat flux for five selected cases with decreasing Rayleigh number from top to bottom: (a) $f = 0.8$, $Ra_m = 7.65 \times 10^7$, $\Delta\eta = 10^8$; (b) $f = 0.8$, $Ra_m = 5.51 \times 10^6$, $\Delta\eta = 10^5$; (c) $f = 0.867$, $Ra_m = 2.2 \times 10^6$, $\Delta\eta = 10^5$; (d) $f = 0.9$, $Ra_m = 2.44 \times 10^6$, $\Delta\eta = 10^6$; and (e) $f = 0.7$, $Ra_m = 1.32 \times 10^6$, $\Delta\eta = 10^6$.

denoted with horizontal dashed lines. Figure 4b shows that for fixed viscosity contrast, the temperature of the well-mixed interior, θ_m , decreases with increasing curvature (decreasing f). Figure 5b further

the characteristic temperature difference, the nondimensional times for the growth of instabilities in the bottom and top conductive layers are

$$t_{\text{bot}} = \frac{4f^2}{\pi} \left(\frac{\delta T_{\text{bot}}}{Nu} \right)^2, \quad (13)$$

$$t_{\text{top}} = \frac{4}{\pi f^2} \left(\frac{\delta T_0}{Nu} \right)^2,$$

where Nu is the time-averaged Nusselt number (also equivalent to the nondimensional heat flux) while δT_{bot} and δT_0 are the nondimensional temperature jumps across the bottom TBL and the layer formed by the top TBL and the stagnant lid, respectively. To a good approximation, $\delta T_{\text{bot}} = (1 - \theta_m)$ and $\delta T_0 = \theta_m$, with θ_m the time-averaged temperature of the well-mixed interior. Table 2 shows that Nu increases with increasing Ra_m and, for a given value of Ra_m , decreases with $\Delta\eta$. Therefore, both t_{top} and t_{bot} decrease with increasing Ra_m and decreasing $\Delta\eta$. Because $f < 1$, and because for all cases in the stagnant lid regime δT_0 is larger than δT_{bot} (Table 2), t_{top} is larger than t_{bot} . In summary, instabilities grow faster with increasing Ra_m and decreasing $\Delta\eta$ and faster in the bottom TBL than in the top conductive layer. The high-frequency variations in the heat flux observed in the bottom TBL (Figure 2) may be explained by the short time required for instabilities to grow.

For a given curvature, the effective Rayleigh number, Ra_m , has an influence on the thickness of the stagnant lid and the convective pattern (Figure 3). When the effective Rayleigh number increases, the total number of plumes increases and the thickness of the stagnant lid decreases.

The horizontally averaged profile of vertically advected heat, $U_z T$, and temperature provides further information about the structure of the shell (Figures 4 and 5). The vertically advected heat vanishes at the top of the system where the heat transfer is purely conductive. Following *Davaille and Jaupart* [1993], we determined the thickness of the stagnant lid from the depth at which the tangent at the inflection point in the $u_z T$ profiles intersects the vertical axis. In Figures 4 and 5, these depths are

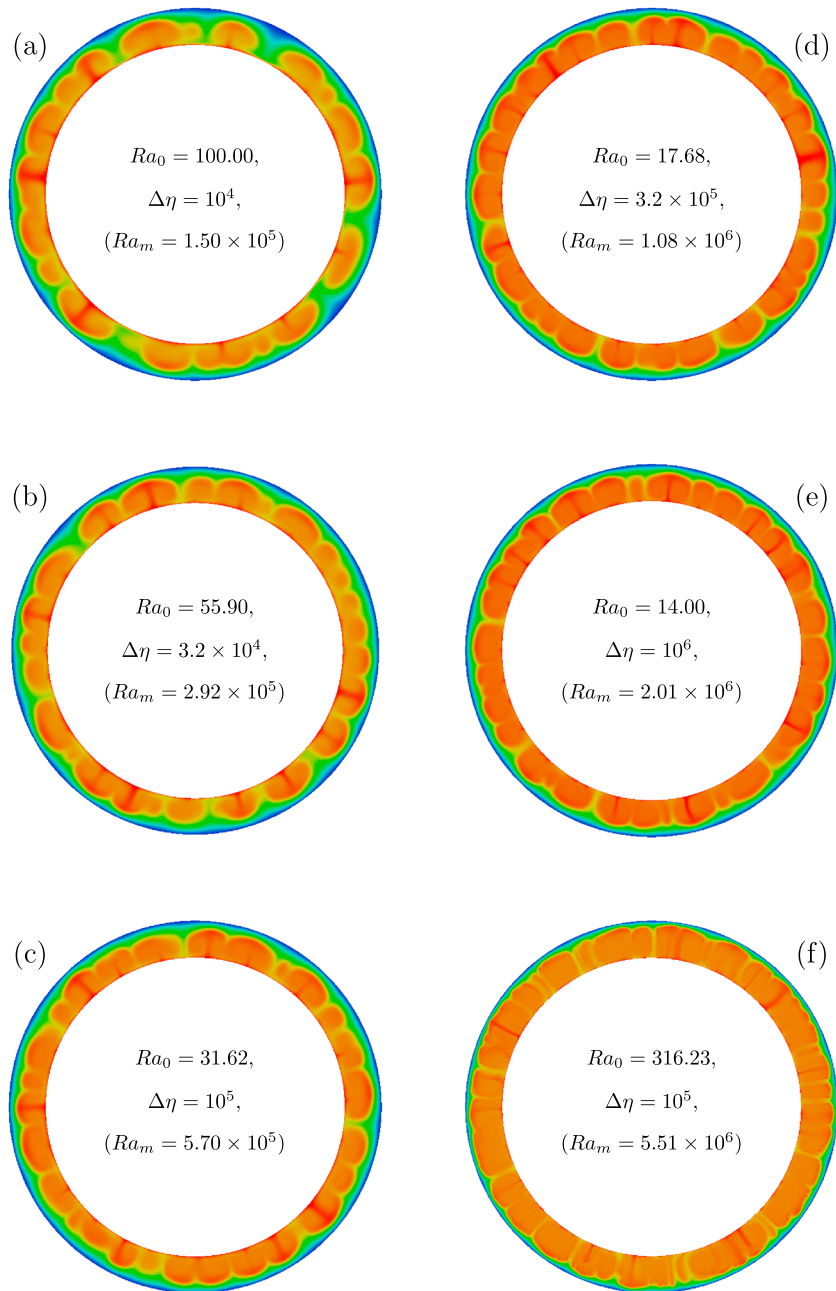


Figure 3. Polar slices of temperature field for $f = 0.8$ and various Ra_m .

shows that for a fixed value of f , θ_m increases with increasing viscosity contrast but does not depend on the Rayleigh number. For a given viscosity contrast and surface Rayleigh number, the thickness of the lid increases with decreasing f (Figure 4a). Nevertheless, it is important to note that the effective Rayleigh number is not the same for all these cases, but decreases with f (Table 2), due to the fact that θ_m decreases with f . Additional cases with same Ra_m and viscosity contrast but different f show that the thickness of the lid decreases with decreasing f (as indicated in Table 2 by cases $Ra_m = 2.4 \times 10^6$ and $\Delta\eta = 10^6$ for $f = 0.9$, $f = 0.8$, and $f = 0.7$). Figure 5a shows that the lid thickness strongly decreases with increasing effective Rayleigh number. Overall, for fixed values of viscosity contrast and effective Rayleigh number, the thickness of the lid decreases with decreasing f .

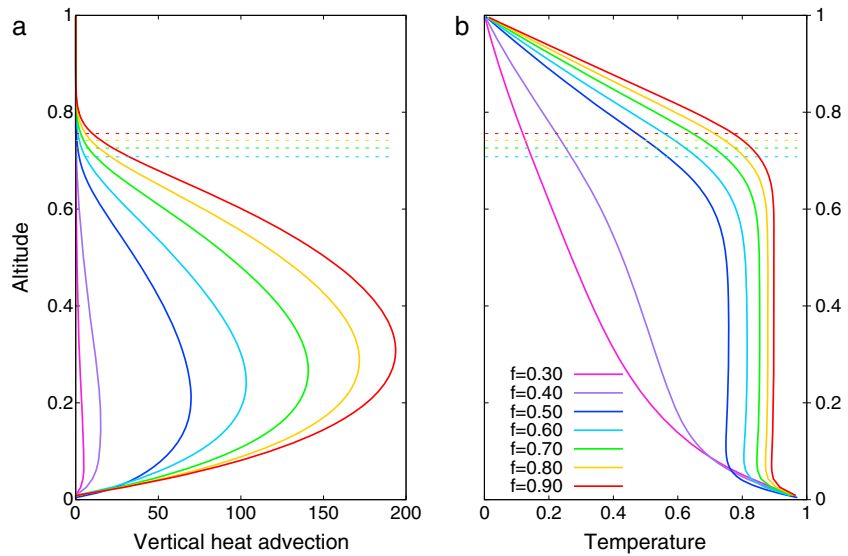


Figure 4. Horizontally averaged profiles of (a) vertical heat flow and (b) temperature for $Ra_0 = 10.0$, $\Delta\eta = 10^6$, for various curvatures. Horizontal dashed lines represent the thickness of the conductive lid.

4. Scaling Laws

Numerical studies for a bottom-heated fluid with strong temperature-dependent viscosities have already been performed in 2-D and 3-D Cartesian geometry from which scaling laws have been determined [Moresi and Solomatov, 1995; Deschamps and Sotin, 2000; Deschamps and Lin, 2014]. Reese et al. [2005] inferred scalings from experiments in spherical shells, but these experiments considered volumetrically heated fluids and one shell curvature ($f = 0.55$) only. Even though a Cartesian geometry is suitable to model a thin ice layer (low curvature), a spherical geometry is required to provide more realistic models for shells that are thicker relative to the core radius (high curvatures). Likewise, 2-D models are not sufficient to model 3-D flow patterns. 3-D spherical geometry provides more realistic models and therefore more accurate scaling laws.

4.1. Internal Temperature

Assuming that in the stagnant lid regime, and for a fluid heated from below, the convective layer (shell below conductive lid) nearly behaves like an isoviscous fluid [Moresi and Solomatov, 1995], and the mean

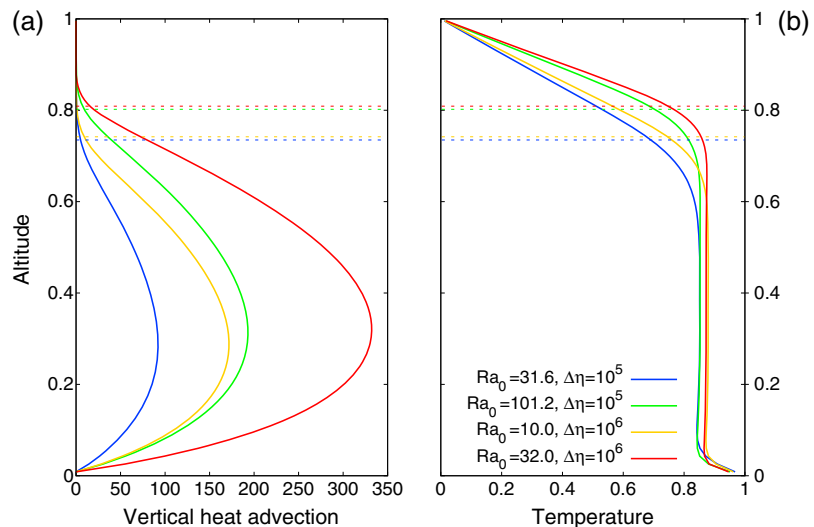


Figure 5. Horizontally averaged profiles of vertical heat flow and temperature for $f = 0.8$ and various Ra_0 and $\Delta\eta$. Horizontal dashed lines represent the thickness of the conductive lid.

nondimensional temperature rescaled to the convective layer, θ_{CL} , obeys

$$\delta T_0 = \theta_{CL}, \quad (14)$$

$$\delta T_{bot} = (1 - \theta_{CL}), \quad (15)$$

where δT_0 and δT_{bot} are the temperature jumps across the top and bottom TBL. Using the temperature scaling for a spherical shell from *Deschamps et al.* [2010], the temperature rescaled to the convective layer is given by

$$\theta_{CL} = \frac{f_{CL}^2}{1 + f_{CL}^2}, \quad (16)$$

where f_{CL} is the ratio between the radius of the core and the radius at the base of the stagnant lid. Dividing equation (15) by equation (14) and inserting equation (16), we obtain

$$\delta T_{bot} = \frac{1}{f_{CL}^2} \delta T_0. \quad (17)$$

The curvature of the convective layer can also be expressed as a function of the curvature of the whole layer through

$$f_{CL} = \frac{f}{1 - (1 - f)d_{lid}}, \quad (18)$$

where d_{lid} is the nondimensional stagnant lid thickness.

We then assume that the temperature jump across the top thermal boundary layer scales as a viscous temperature scale ΔT_v , as suggested by *Davaille and Jaupart* [1993]

$$\delta T_0 = a \left(\frac{\Delta T_v}{\Delta T} \right), \quad (19)$$

where $\Delta T_v = -\frac{\eta(T_m)}{\frac{d\eta}{dT}|_{T=T_m}}$ with T_m the temperature of the well-mixed interior. According to equation (2), the viscous temperature scale depends on the logarithmic viscosity contrast through the relation $\Delta T_v = \Delta T/\gamma$.

Combining equation (17) to equation (19), and using the temperature difference across the convective layer, we obtain

$$\delta T_{bot} = a \frac{[1 - (1 - f)d_{lid}]^2}{f^2} \left(\frac{\Delta T_v}{\Delta T} \right), \quad (20)$$

with ΔT the temperature difference across the system.

The nondimensional form of the conductive temperature profile in a spherical shell of unit depth with isothermal boundaries is

$$\theta(r) = RF_{top} \left(\frac{R}{r} - 1 \right), \quad (21)$$

where r is the radius and R is the outer radius of the spherical shell. Noting that $r_{lid} = (R - d_{lid})$, the nondimensional temperature at the base of the conductive lid can be written as

$$\theta_{lid} = \frac{d_{lid}}{1 - (1 - f)d_{lid}} F_{top}, \quad (22)$$

and d_{lid} can be expressed as a function of the nondimensional heat flux at the surface F_{top} and the temperature at the bottom of the lid θ_{lid} so that

$$d_{lid} = \frac{\theta_{lid}}{F_{top} + (1 - f)\theta_{lid}}. \quad (23)$$

Replacing d_{lid} by its expression (equation (23)), equation (20) becomes

$$\delta T_{bot} = \frac{a}{f^2} \frac{F_{top}^2}{[F_{top} + (1 - f)\theta_{lid}]^2} \left(\frac{\Delta T_v}{\Delta T} \right). \quad (24)$$

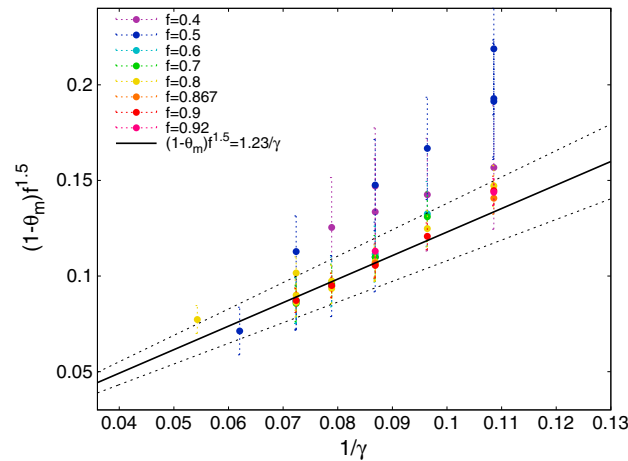


Figure 6. Nondimensional temperature jump across the lower thermal boundary layer as a function of the parameter γ . The black line corresponds to the inverted scaling law, and the dashed lines give the error around the fit. Only cases with $f > 0.5$ were used to invert the data.

dimensional temperature difference across the bottom thermal boundary layer is well related to curvature and the viscosity contrast by

$$(1 - \theta_m) = \frac{\alpha_T}{\gamma f^\beta}. \quad (26)$$

To invert data in Table 2, we used a nonlinear generalized inverse method [Tarantola and Valette, 1982], which allows estimation of error bars in the output parameters. Inversion of our results leads to $\alpha_T = 1.23 \pm 0.15$ and $\beta = 1.5 \pm 0.22$. Note that only cases in the stagnant lid regime were used in the inversion. The uncertainties are computed assuming a relative uncertainty on the average temperature of 0.5%, which corresponds to the average amplitude of the oscillation around its mean value during the quasi-stationary phase.

Figure 6 shows that cases at $f \geq 0.6$ fit better in the error bars than cases with low f . When f is low, the stagnant lid regime requires a larger viscosity contrast (section 5) to operate. Again, these cases were not used for the inversion. We also note that cases with $1/\gamma \leq 0.1$ do not fit the scaling law. Those cases correspond to lower values of the thermal viscosity contrast, and thus, the conductive lid may not be well developed.

Our scaling provides the internal temperature in the ice shell for a given curvature (layer thickness relative to core radius) and viscosity contrast and indicates that the temperature increases with increasing viscosity contrast and decreases with increasing shell's curvature (decreasing f).

4.2. Heat Flux

The efficiency of the heat transfer is determined by the Nusselt number, which results from the competition between two effects. With increasing viscosity contrast, the temperature of the well-mixed interior increases and the bulk viscosity calculated with this temperature decreases. This in turn increases the effective Rayleigh number. In contrast, the presence of the stagnant lid insulates the convective layer and thus decreases the heat transfer to the surface. Another effect is that the ΔT that participates in convection decreases, reducing the vigor of convection in the convective layer. Previous studies using 2-D Cartesian numerical experiments [Moresi and Solomatov, 1995; Deschamps and Sotin, 2000] showed that the second effect is dominant, and the Nusselt number strongly decreases with increasing viscosity contrast. For an isoviscous fluid, the nondimensional heat flux across a TBL scales as

$$q = a' Ra^{b'} \delta T_{TBL}^{c'} \quad (27)$$

where δT_{TBL} is the temperature across the TBL [Sotin and Labrosse, 1999; Shahnas et al., 2008] and a' , b' , c' are constant values. For fluids including viscosity contrast, the temperature across the bottom boundary layer

For large values of f ($f > 0.5$), it can be assumed that $(1 - f)\theta_{lid}/F_{top} \ll 1$. Using this approximation, equation (24) can be simplified to

$$\delta T_{bot} = \frac{a}{f^2} \left(\frac{\Delta T_V}{\Delta T} \right). \quad (25)$$

This analysis provides a power law relationship between the nondimensional temperature jump across the bottom TBL and the inverse of the curvature with an exponent of 2, which can be tested with our data (Table 2).

We thus invert the results of our numerical experiments to determine scaling laws for the temperature jump across the bottom TBL (Figure 6). The parameters are determined by a least squares fit of the data in Table 2. The nondimen-

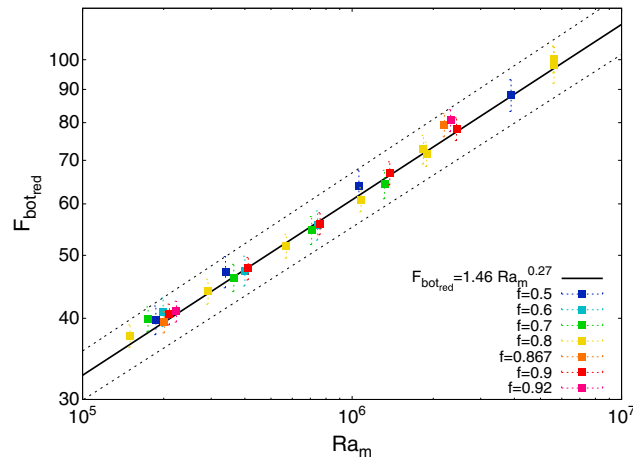


Figure 7. Reduced bottom heat flux, $F_{\text{bot,red}} = F_{\text{bot}}\gamma^{1.21}f^{1.78}$, as a function of the effective Rayleigh number. The black line corresponds to the inverted scaling law, and the dashed lines give the error around the fit.

is given by equation (26). Replacing Ra by the effective Rayleigh number Ra_m , equation (27) can be used to parameterize the heat flux, F_{bot} , at the bottom of the system with

$$F_{\text{bot}} = \frac{a_f Ra_m^b}{\gamma^c f^d} \quad (28)$$

The nondimensional heat flux at the top of the fluid may be obtained from equation (9). Furthermore, according to equation (11), the Nusselt number is simply

$$Nu = \frac{a_f Ra_m^b}{\gamma^c f^{(d-1)}} \quad (29)$$

Using the stagnant lid regime cases listed in Table 2, we find that the best fit solution corresponds to $a_f = 2.01 \pm 0.26$, $b = 0.30 \pm 0.01$, $c = 1.50 \pm 0.01$, and $d = 1.91 \pm 0.03$. However, the trade-off between parameters is significant (the covariance between a_f and c is up to 0.8); thus, we decided to calculate a specific solution that fits 3-D Cartesian geometry results (i.e., for $f = 1.0$). The values of a_f and b are prescribed to be consistent with the law obtained by *Deschamps and Lin* [2014]. Accordingly, the parameters become $a_f = 1.46$, $b = 0.27$, $c = 1.21 \pm 0.01$, and $d = 1.78 \pm 0.02$. This scaling law (Figure 7) fits our data points very well. For comparison with scalings obtained in 3-D Cartesian geometry, it is convenient to use the Nusselt number, which, following equation (29), scales as $Nu \propto f^{-0.78}$. Both scaling laws are compared to 2-D Cartesian, 3-D Cartesian, and 2-D spherical parameterization in Table 3. Our 3-D spherical scalings use the 3-D Cartesian scalings of *Deschamps and Lin* [2014] as boundary conditions for $f = 1$ and are therefore fully consistent with these scalings. The comparison between 2-D Cartesian and 3-D Cartesian scalings shows substantial differences (see *Deschamps and Lin* [2014] for a detailed comparison), with the 3-D Cartesian scalings predicting larger heat flux by up to 20–40% compared to those resulting from 2-D Cartesian scalings. The determined scaling relationship gives an important constraint on the heat loss and thus on the cooling rate of the satellite for a given curvature, Rayleigh number, and viscosity contrast. Interestingly, equation (29), together with the inverted value of d , indicates that the Nusselt number (and thus the efficiency of heat transfer) increases with increasing curvature (decreasing f), all other parameters being equal. For a given thermal viscosity contrast, the effect of the conductive lid is therefore less strong as the shell's curvature increases (section 5). Strictly speaking, our scalings are valid only for values of f larger than or equal to 0.4. Because none of our experiments with $f \leq 0.4$ operate in the stagnant lid regime, we did not take them into account to invert the scaling law parameters. If, as discussed in section 5, the development of the stagnant lid regime depends on curvature

Table 3. Comparison Between Parameterized Laws in Different Geometries

References	Geometry	θ_m	Nu
<i>Moresi and Solomatov</i> [1995]	2-D Cartesian	$(1 - \theta_m) = \frac{1.1Ra_m^{-0.04}}{\gamma^{0.73}}$	$Nu = \frac{1.89Ra_m^{0.2}}{\gamma^{1.02}}$
<i>Deschamps and Sotin</i> [2000]	2-D Cartesian	$(1 - \theta_m) = \frac{1.43}{\gamma} - 0.03$	$Nu = \frac{3.8Ra_m^{0.258}}{\gamma^{1.63}}$
<i>Dumoulin et al.</i> [1999]	2-D Cartesian		$Nu = \frac{0.52Ra_m^{1/3}}{\gamma^{4/3}}$
<i>Reese et al.</i> [2005]	2-D Spherical		$Nu = \frac{0.67Ra_m^{1/3}}{\gamma^{4/3}}$
<i>Deschamps and Lin</i> [2014]	3-D Cartesian	$(1 - \theta_m) = \frac{1.23}{\gamma}$	$Nu = \frac{1.46Ra_m^{0.27}}{\gamma^{1.21}}$
This study	3-D Spherical	$(1 - \theta_m) = \frac{1.23}{\gamma f^{1.5}}$	$Nu = \frac{1.46Ra_m^{0.27}}{\gamma^{1.21}f^{0.78}}$

and is obtained for larger values of $\Delta\eta$ as curvature increases, our scaling may be used for $f \leq 0.4$, provided that the viscosity contrast is large enough. On the other hand, one cannot exclude the possibility that convection does not operate in the stagnant lid regime for low values of f . Additional calculations are needed to clarify this point and map in detail the boundary between the stagnant lid and weak regimes as a function of f and $\Delta\eta$.

5. Influence of Curvature on Stagnant Lid Convection

A decrease in average temperature with increasing curvature (i.e., decreasing f) is well documented for isoviscous shells [Jarvis *et al.*, 1995; Shahnas *et al.*, 2008; Deschamps *et al.*, 2010]. Our calculations indicate that this decrease also holds for strongly temperature-dependent viscosity shells (equation (26)). Interestingly, our results further show that this decrease influences the development of the stagnant lid. The cooling of the convecting shell induced by decreasing f is accompanied by attrition of the thermal gradient across the upper thermal boundary layer. Consequently, the viscosity contrast between the surface and the underlying fluid is reduced so that the stagnant lid is weaker or, if f is small enough, cannot form, as it would in a case with a warmer interior. Stagnant lid convection is therefore more likely to operate in shells with small curvature (i.e., corresponding to a large core radius compared to the mantle or ice shell thickness), rather than in shells with large curvature and will be easiest to obtain in plane layer convection ($f = 1$) [O'Farrell *et al.*, 2013].

For cases operating in the stagnant lid regime, and for fixed viscosity contrast and Rayleigh number, the lid thins with increasing curvature, and its effect on the heat transfer is weaker. The transported heat flux, measured by the Nusselt number, $Nu = f \times F_{\text{bot}}$, increases with increasing curvature (decreasing f), as indicated by equation (29). For example, compared to the 3-D Cartesian case ($f = 1$), with $d = 1.78$ in equation (29), the convective heat flux is larger by 20% for $f = 0.8$ and 70% for $f = 0.5$.

As f decreases, and for a given viscosity contrast, transition to the stagnant lid regime requires greater reference Ra (e.g., Ra_0 or Ra_{bot}). Increasing the Rayleigh number for a fixed f value increases the thermal gradient and therefore the viscosity gradient between the surface and interior, more readily enabling decoupling of the surface and interior flow.

Different regime characteristics are indicated by the time-averaged temperature profile, as shown in Figure 8a. In the marginally critical convection regime, the temperature profile is almost conductive and the isosurface shows only one plume (for $f = 0.3$). In order to identify the transition region where stagnant lid convection appears at low curvatures, we investigated a number of cases featuring $f < 0.5$ values. The results are included in Table 2.

Figure 8b shows that depending on the curvature f , the stagnant lid regime does not appear for the same values of Ra_{bot} and $\Delta\eta$. For Ra_{bot} equal to 3.16×10^6 and $\Delta\eta$ equal to 10^5 , the $f = 0.3$ case is only weakly convecting, whereas the cases at $f = 0.4$ and $f = 0.5$ develop clearly identifiable thermal boundary layers separated by a nearly isothermal region and the cases with $f \geq 0.6$ are in the stagnant lid regime. The case with $f = 0.3$ is typical of convection with small f values found for isoviscous fluids, which show only one or two plumes being able to form on the relatively small surface area core [Jarvis *et al.*, 1995]. We find that for $f \leq 0.5$, as viscosity contrast is decreased a transition occurs from marginally critical convection to weak convection in which an isothermal interior appears and finally stagnant lid regime convection, in which plume number increases. The latter observation is consistent with the effective f increasing, as determined by the thicknesses of the vigorously convecting layer below the surface layer, relative to the core radius.

Our finding that an increase in viscosity contrast can increase surface mobility appears contrary to the fact that a strong viscosity contrast is the key requirement of the stagnant lid regime. In fact, our findings suggest that for small f stagnant lid convection occurs for a range of viscosity contrasts bounded by lower and upper threshold values. For small values of f , the cold temperatures through a great extent of the fluid layer keep the viscosity at high values to such depth that a distinct high-viscosity lid cannot form (see Figure 4). Instead, the majority of the spherical shell remains cold and viscously coupled, convecting at very low vigor. However, as noted above, an increase in Rayleigh number carries more heat radially, warming the interior and allows a sharper viscosity contrast to develop between the outer layer of the sphere and the interior. For example, when Ra_{bot} increases to 3.2×10^6 and $\Delta\eta$ is 10^4 , the previous $f = 0.5$ case shown in Figure 8b enters

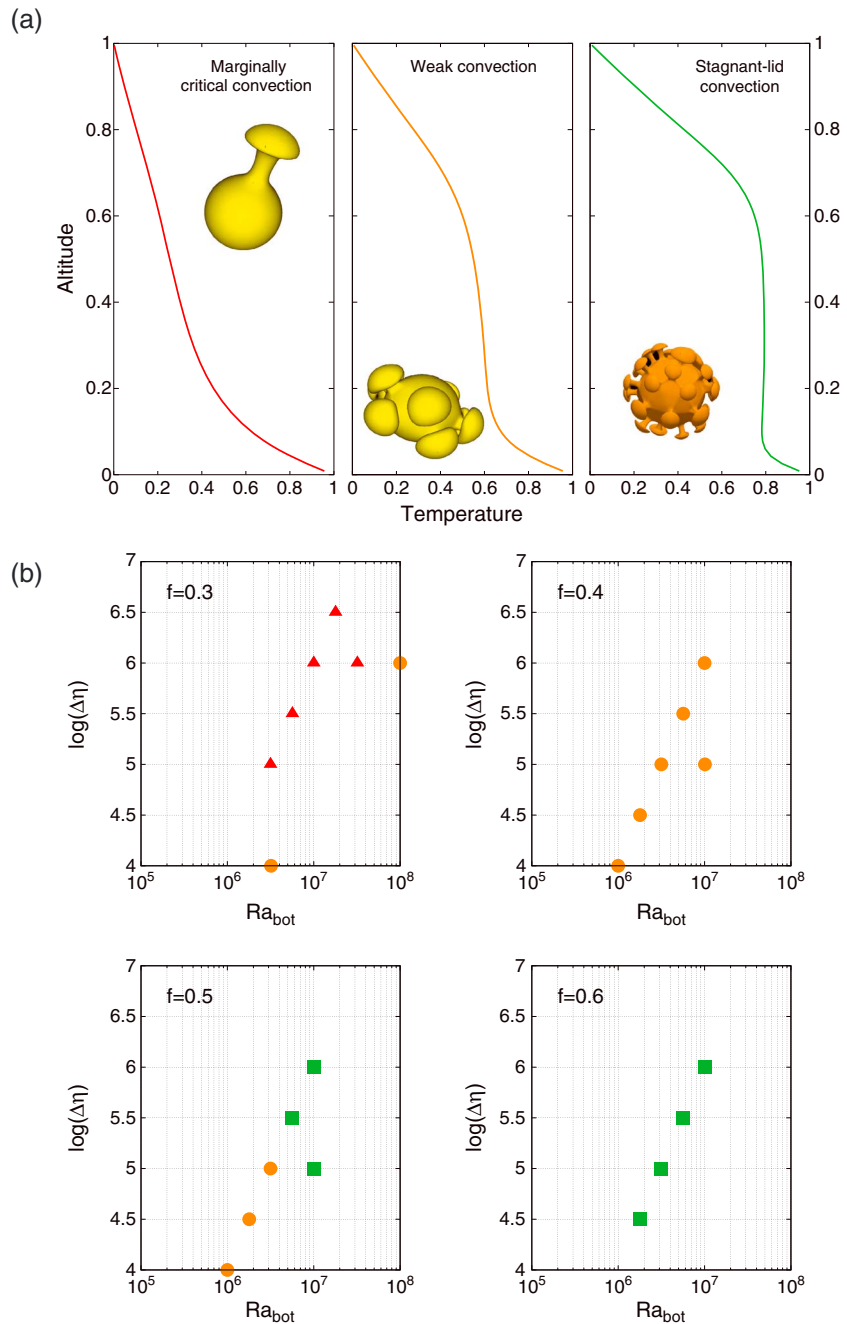


Figure 8. (a) Typical temperature vertical profile and isosurface for marginally critical ($f = 0.30, Ra_0 = 31.62, \Delta\eta = 10^5$), weak ($f = 0.50, Ra_0 = 31.62, \Delta\eta = 10^5$), and stagnant lid ($f = 0.60, Ra_0 = 31.62, \Delta\eta = 10^5$) convecting cases. (b) Location of the different convective regimes. Green squares correspond to stagnant lid regime, orange dots to weak convection, and red triangles to marginally critical convection. Ra_{bot} is the Rayleigh number at the bottom of the box and can be written as $Ra_{bot} = Ra_{1/2} \exp(\gamma/2)$.

the stagnant lid regime. Thus, stagnant lid convection can be obtained with small f but requires a higher Rayleigh number.

6. Application to the Outer Ice Shell of Pluto and Europa

The scalings we obtained from our numerical experiments (section 4) can be used to model the structure and evolution of dwarf planets and icy satellites. Here we only outline a method to calculate the average

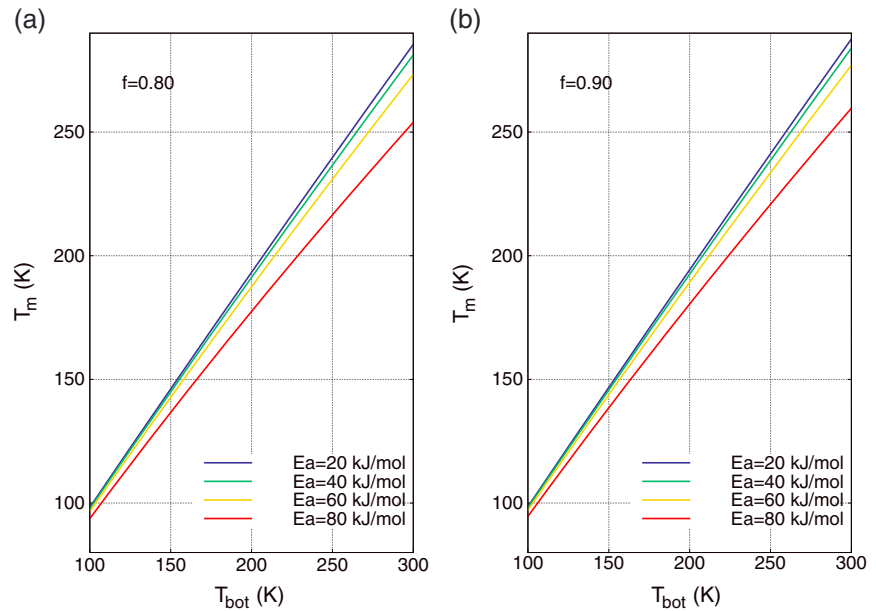


Figure 9. Temperature of the well-mixed interior as a function of the temperature at the bottom.

temperature of the outer ice I layer and the heat flux through this layer at a given time, but we do not attempt to reconstruct its thermal and radial evolution.

A possible internal structure for both icy satellites and dwarf planets consists of a large silicate core, surrounded by a high-pressure ice layer, a liquid ocean, and an ice I shell [Lewis, 1971]. If the heat transfer through this outer layer is efficient enough, the liquid layer may fully crystallize forming a continuous ice layer. Therefore, the heat transfer plays a fundamental role in the thermal and structural evolution of the body. Another important parameter is the initial chemical composition of the subsurface ocean. In particular, the presence of an antifreeze compound (ammonia, for instance) lowers the crystallization temperature of the ocean. Combined with phase diagrams of the water or water + volatile systems, the scaling laws inferred in section 4 can be used to model the heat transfer through the outer ice shell of icy bodies.

The viscosity of ice I depends strongly on temperature and is well described by an Arrhenius law

$$\eta(T) = \eta_{\text{ref}} \exp \left[\frac{E_a}{\mathcal{R}T_{\text{ref}}} \left(\frac{T_{\text{ref}}}{T} - 1 \right) \right], \quad (30)$$

where E_a is the activation energy of ice I, \mathcal{R} is the ideal gas constant, and η_{ref} is the viscosity at a reference temperature T_{ref} . Here we used $\eta_{\text{ref}} = 5.0 \times 10^{13} \text{ Pa} \cdot \text{s}$ [Deschamps and Sotin, 2001], a value deduced from stress/strain curves measured for alpine glaciers [Gerrard et al., 1952].

The scalings obtained in section 4 are relating nondimensional properties of the system and should be rescaled according to the planet or body properties. The scaling law for internal temperature (equation(26)) can be rescaled as a function of the temperature at the bottom of the ice layer

$$T_m = T_{\text{bot}} - \frac{1.23}{f^{1.5}} \Delta T_v, \quad (31)$$

where T_{bot} is the temperature at the bottom of the ice I layer. According to equation (30), the viscous temperature scale can be expressed as

$$\Delta T_v = \frac{\mathcal{R}T_m^2}{E_a}. \quad (32)$$

The temperature of the well-mixed interior, T_m , can be computed by inserting equation (32) in equation (31). T_m is then the positive solution of the resulting second order polynomial. Figures 9 shows the temperature of the well-mixed interior as a function of the temperature at the bottom of the shell, T_{bot} , for several values of the activation energy E_a . For a given value of T_{bot} , the temperature of the well-mixed

Table 4. Properties of Pluto and Europa^a

Parameter	Symbol	Europa	Pluto	Unit
Total radius	R	1560	1153	km
Core radius	R_c	1400	920	km
Average density	ρ	3000	2000	kg/m ³
Gravity acceleration	g	1.31	0.66	m/s ²
Surface temperature	T_0	100	44	K

^aThe core radius is estimated from the average density and a core mean density of 3800 and 3000 kg/m³ for Europa and Pluto, respectively.

($\sim 3.5 \times 10^{-14} \text{ s}^{-1}$), yielding an activation energy of $E_a = 60 \text{ kJ/mol}$. This value will thus be used in the subsequent calculations.

One may point out that the rheology of ice I is non-Newtonian [Goodman *et al.*, 1981], but in our numerical experiments and applications, we assume a Newtonian rheology. Nevertheless, Dumoulin *et al.* [1999] have shown that the effect of non-Newtonian rheology can be reproduced with Newtonian scaling by prescribing smaller (by about a factor 2) activation energy. Figure 9 further shows that the influence of activation energy on the internal temperature is moderate. Decreasing the value of this parameter from 60 to 20 KJ/mol induces a small ($< 10 \text{ K}$) change in T_m . In comparison, the presence of antifreeze compounds in the ocean has a much stronger influence, by imposing the value of T_{bot} .

Both T_{bot} and f depend on the thickness of the ice layer. T_{bot} is by definition the temperature of the liquidus of water (or of the water + volatile mixture) and can be computed from the phase diagram of water at the pressure P_{bot} . Here we performed calculations for a pure water ocean only.

We parameterized the liquidus of water with the relation from Chizhov [1993]

$$T_{\text{bot}} = 273.2 \left(1 - \frac{P_{\text{bot}}}{0.395} \right)^{1/9} \quad (33)$$

with $P_{\text{bot}} = \rho_{\text{ice}} g D$ and $\rho_{\text{ice}} = 917 \text{ kg/m}^3$. This equation corresponds to the interface between ice I and water.

The effective Rayleigh number of the ice I shell depends on the viscosity at T_m

$$Ra_m = \frac{\alpha_l \rho_l g \Delta T D^3}{\eta(T_m) \kappa_l}, \quad (34)$$

where α_l , ρ_l , and κ_l are the thermal expansion, the density and the thermal diffusivity of ice I, respectively. $\Delta T = (T_{\text{bot}} - T_0)$ is the temperature difference across the ice I layer.

The scaling law for the convective heat flux at the bottom of the ice layer described by equation (28) can be rescaled as

$$\Phi_{\text{bot}} = \frac{1.46 Ra_m^{0.27}}{f^{1.78}} \left(\frac{\Delta T_v}{\Delta T} \right)^{1.21} \Phi_c \quad (35)$$

where Φ_c is the conductive heat flux at the bottom. In spherical geometry $\Phi_c = k_l \frac{T_{\text{bot}} - T_0}{Df}$, where k_l is the thermal conductivity of ice I.

Table 5. Properties of Ice I

Parameter	Symbol	Value	Unit
Activation energy	E_a	60	kJ/mol
Reference viscosity	η_{ref}	5×10^{13}	Pa s
Density	ρ_l	917	kg/m ³
Thermal conductivity	k_l	2.6	W/m/K
Thermal expansion	α_l	1.56×10^{-4}	K^{-1}
Thermal diffusivity	κ_l	1.47×10^{-4}	m^2/s

interior increases with increasing activation energy. According to equation (30), a high activation energy value increases the temperature dependence of viscosity and reduces the heat transfer through the shell. Activation energy can be evaluated from laboratory flow experiments. Durham *et al.* [2010] determined that dislocation creep laws apply to a temperature range of roughly 150–250 K at planetary strain rates

($\sim 3.5 \times 10^{-14} \text{ s}^{-1}$), yielding an activation energy of $E_a = 60 \text{ kJ/mol}$. This value will thus be used in the subsequent calculations.

Both T_{bot} and f depend on the thickness of the ice layer. T_{bot} is by definition the temperature of the liquidus of water (or of the water + volatile mixture) and can be computed from the phase diagram of water at the pressure P_{bot} . Here we performed calculations for a pure water ocean only.

We parameterized the liquidus of water with the relation from Chizhov [1993]

$$T_{\text{bot}} = 273.2 \left(1 - \frac{P_{\text{bot}}}{0.395} \right)^{1/9} \quad (33)$$

with $P_{\text{bot}} = \rho_{\text{ice}} g D$ and $\rho_{\text{ice}} = 917 \text{ kg/m}^3$. This equation corresponds to the interface between ice I and water.

The effective Rayleigh number of the ice I shell depends on the viscosity at T_m

$$Ra_m = \frac{\alpha_l \rho_l g \Delta T D^3}{\eta(T_m) \kappa_l}, \quad (34)$$

where α_l , ρ_l , and κ_l are the thermal expansion, the density and the thermal diffusivity of ice I, respectively. $\Delta T = (T_{\text{bot}} - T_0)$ is the temperature difference across the ice I layer.

The scaling law for the convective heat flux at the bottom of the ice layer described by equation (28) can be rescaled as

$$\Phi_{\text{bot}} = \frac{1.46 Ra_m^{0.27}}{f^{1.78}} \left(\frac{\Delta T_v}{\Delta T} \right)^{1.21} \Phi_c \quad (35)$$

where Φ_c is the conductive heat flux at the bottom. In spherical geometry $\Phi_c = k_l \frac{T_{\text{bot}} - T_0}{Df}$, where k_l is the thermal conductivity of ice I.

To illustrate the effect of the curvature on the temperature and heat flux, we apply equations (31)–(35) to Europa and Pluto. The maximum ice I thickness, given by the difference between the total and core radii, is 160 km for Europa and 230 km for Pluto, corresponding to values of f around 0.9 and 0.8, respectively. The properties of Pluto and Europa and the properties of ice I are listed in Tables 4 and 5. Note that in the case of Europa, internal heating resulting from tidal

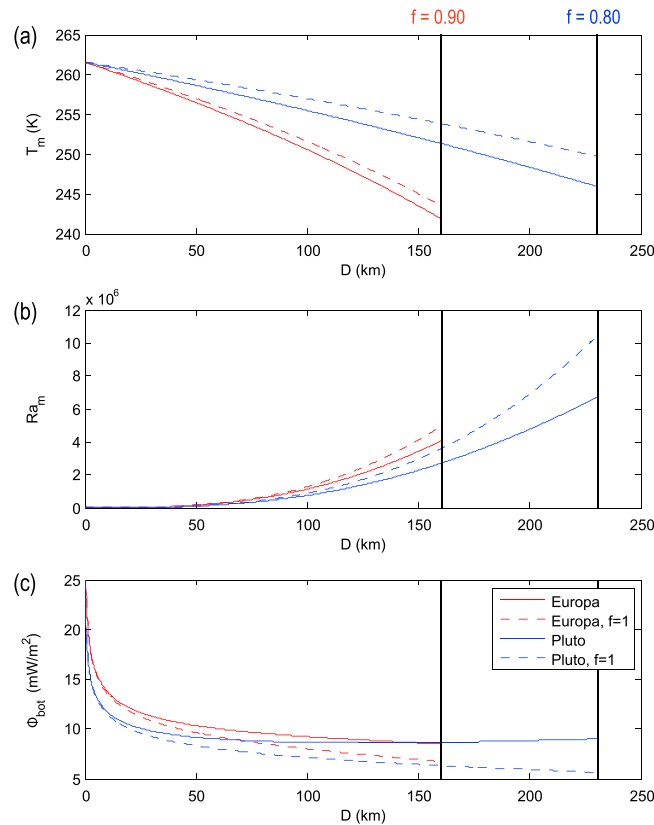


Figure 10. (a) Temperature of the well-mixed interior, (b) effective Rayleigh number, and (c) heat flux at the bottom for Europa and Pluto as a function of the thickness of the ice I layer for a variable f (solid line) and for $f = 1$ (dashed line). The vertical thick lines denote the maximum thickness of ice I layer, i.e., $R - R_c$.

the ice I layer thickens is related to the fact that T_{bot} (equal to the temperature of the liquidus) decreases with increasing depth. However, the increase in curvature induces a small additional drop in temperature, as indicated by the difference between the 3-D Cartesian (dashed curves) and 3-D spherical (solid curves) scalings, which increases with D (thus with decreasing f) (Figure 10a). The effective Rayleigh number naturally increases with the layer thickness (equation (34)). It further increases due to the drop in the bottom temperature, which leads to larger ΔT . The decrease in the temperature of the well-mixed interior, which increases the viscosity, partially compensates these effects. As a result of the temperature drop increasing with f , taking into account the variation of the shell curvature leads to smaller Rayleigh number (Figure 10b). Moreover, because it depends on the conductive heat flux (equation (35)), the convective heat flux decreases as the ice I layer thickens. As discussed in section 5, the stagnant lid is less developed as the curvature increases, i.e. as the ice layer thickens, all other parameters being equal. As a result, the heat transfer is more efficient if the curvature is taken into account (Figure 10c). The difference reaches about 20% in the case of Europa and 50% in the case of Pluto. Interestingly, in the case of Pluto, the heat flux decrease is fully compensated by the curvature effect if the ice layer is thick enough (150 km and more). Variations in the curvature of the outer ice shell of Europa and Pluto, as these shells crystallize, may thus have nonnegligible effects on the thermal evolution of the icy moons and dwarf planet and should therefore be taken into account.

7. Concluding Discussion

The numerical experiments of convection in spherical shells we performed indicate that the curvature (or, equivalently, the relative size of the shell compared to the underlying core measured by the

dissipation in the ice I layer may have played an important role in the evolution of its radial structure [Tobie *et al.*, 2003]. We do not account for this effect in the calculations below.

The phase diagram of water [Chizhov, 1993] shows a transition from ice I to ice III at a pressure of 0.207 GPa. For large bodies (e.g., Ganymede and Titan), this transition leads to a more complex radial structure, since a layer of high-pressure ice may be present between the residual ocean and the core. However, such high-pressure ice layers are unlikely to exist in Europa and Pluto, since in both cases the transition pressure from ice I to ice III would be within the core.

Figure 10 shows the temperature of the well-mixed interior (equations (31) and (32)), the effective Rayleigh number (equation (34)) and the convective heat flux at the bottom of the outer ice shell (equation (35)) as a function of the thickness D of this shell. The curvature increases (f decreases) with the thickening of the ice I shell. For comparison, we also plotted the heat flux predicted by 3-D Cartesian scalings, i.e., by setting $f = 1$ independently of D in equations (31) and (35). The decrease in temperature as

ratio f) strongly influences the mode in which convection operates. Depending on the Rayleigh number, curvature, and thermal viscosity contrast, we identify three different regimes. Our results show that for a thick shell relative to the core radius (i.e., low f), the stagnant lid regime is more difficult to obtain and appears only if the Rayleigh number is large enough. Moreover, a stagnant lid requires a large viscosity contrast, but if it is too high, the shell does not convect at all. For cases in the stagnant lid regime, our results show that the thickness of the lid decreases with increasing curvature (decreasing f), all other properties being similar. Accordingly, the efficiency of heat transfer increases with increasing curvature.

Our numerical experiments allow us to build scaling laws for the average temperature of the well-mixed interior (i.e., excluding the stagnant lid) and for the convective heat flux. The average temperature of the well-mixed interior depends only on the viscosity contrast and curvature, decreasing with increasing curvature. The heat flux further depends on the vigor of convection and, as already pointed out, increases with increasing curvature. Combined with experimentally determined melting curves, these scaling laws can be used to investigate the thermal histories and radial structures of icy moons and dwarf planets.

The outer ice I layers of icy moons and dwarf planets result from the crystallization of their primordial ocean [e.g., *Hussmann et al.*, 2007]. These layers first transfer heat by conduction, but when they are thick enough, typically a few tens of kilometers, they become unstable and are animated by convection. Crystallization stops if convection in the ice I layer is not efficient enough to transfer to the surface the heat available at its base. Today, the thickness of the outer ice I shell should not exceed a few hundreds of kilometers, leading to values of f around 0.8 or larger. Thus, convection in the ice I layers of icy moons has likely operated in the stagnant lid regime throughout the histories of these bodies. As the ice I layer thickens its curvature increases, which, according to our results, reduces the thickness of the stagnant lid (relatively to the total thickness of the ice I layer) and significantly improves the heat transfer by convection. This partially compensates the reduction of the heat flux induced by the presence of antifreeze compounds and may thus slightly delay the crystallization shut-off.

Our numerical experiments, and the derived scaling laws, assume a number of simplifications, which should be kept in mind when applying them to icy layers. As discussed in section 6, at the condition of stress and pressure of the icy moons, the rheology of ice I is non-Newtonian [*Goodman et al.*, 1981], whereas our experiments assume a Newtonian rheology. This difficulty can be addressed by prescribing lower values of the activation energy, as suggested by *Dumoulin et al.* [1999]. Because compared to other parameters, particularly the presence of antifreeze compounds in the primordial ocean, activation energy has a limited influence on convection in the ice I layer [*Deschamps and Sotin*, 2001] (this study, Figure 9), uncertainty on its value is not a crucial issue. Similarly, our experiments do not account for pressure dependence of the viscosity. This approximation, however, is certainly valid in the case of the ice I layer of icy bodies, where the pressure remains small, 0.21 GPa at most. More importantly, in our experiments shells are heated from their base only. In isoviscous fluids, the addition of internal heating has strong effects on the flow, by weakening the bottom thermal boundary layer and thus the growth of hot plumes [e.g., *Travis and Olson*, 1994; *Sotin and Labrosse*, 1999; *Shahnas et al.*, 2008; *Deschamps et al.*, 2010]. As the amount of internal heating increases, convection is dominated by downwellings. In the case of icy moons, internal heating resulting from tidal dissipation may be important for bodies that have not reached a synchronous spin. The results from *Tobie et al.* [2005] show that the average value of tidal heating in the ice I shell is typically around 10^{-10} W/kg (corresponding to nondimensional rate of internal heating around 5). Numerical experiments for an isoviscous fluid in various geometries [*Travis and Olson*, 1994; *Sotin and Labrosse*, 1999; *Shahnas et al.*, 2008; *Deschamps et al.*, 2010] indicate that such amount of internal heating has a moderate effect on the convection pattern. The average temperature and the bottom heat flux (i.e., the flux that can be extracted from the underlying core) are also affected by internal heating, leading to different scaling laws than those obtained for bottom-heated fluid. For stagnant lid convection, however, temperature and heat flux scaling for mixed heating are still to be determined.

References

- Chizhov, V. (1993), Thermodynamic properties and thermal equations of the state of high-pressure ice phases, *J. Appl. Mech. Tech. Phys.*, 34(2), 253–262, doi:10.1007/BF00852521.
- Christensen, U. (1984), Heat transport by variable viscosity convection and implications for the Earth's thermal evolution, *Phys. Earth Planet. Inter.*, 35(4), 264–282, doi:10.1016/0031-9201(84)90021-9.
- Davaile, A., and C. Jaupart (1993), Transient high-Rayleigh-number thermal-convection with large viscosity variations, *J. Fluid Mech.*, 253, 141–166, doi:10.1017/S0022112093001740.

Acknowledgments

We are grateful to the two anonymous colleagues and to the Associate Editor for their constructive reviews and comments, which were useful to improve a first version of this manuscript. This project was supported by grant ETH-03 10-1 from the ETH Research Commission, grant AS-102-CDA-M02 from Academia Sinica (Taiwan), and grant 101-2116-M-001-001-MY3 from National Science Council of Taiwan (NSC). JPL is grateful for funding from the Natural Sciences and Engineering Research Council of Canada (DG-327084-10). Data supporting this article are available in Table 2.

- Deschamps, F., and J.-R. Lin (2014), Stagnant lid convection in 3D-Cartesian geometry: Scaling laws and applications to icy moons and dwarf planets, *Phys. Earth Planet. Inter.*, 229, 40–54, doi:10.1016/j.pepi.2014.01.002.
- Deschamps, F., and C. Sotin (2000), Inversion of two-dimensional numerical convection experiments for a fluid with a strongly temperature-dependent viscosity, *Geophys. J. Int.*, 143(1), 204–218, doi:10.1046/j.1365-246x.2000.00228.x.
- Deschamps, F., and C. Sotin (2001), Thermal convection in the outer shell of large icy satellites, *J. Geophys. Res.*, 106(E3), 5107–5121, doi:10.1029/2000JE001253.
- Deschamps, F., P. J. Tackley, and T. Nakagawa (2010), Temperature and heat flux scalings for isoviscous thermal convection in spherical geometry, *Geophys. J. Int.*, 182(1), 137–154, doi:10.1111/j.1365-246X.2010.04637.x.
- Dumoulin, C., M.-P. Doin, and L. Fleitout (1999), Heat transport in stagnant lid convection with temperature- and pressure-dependent Newtonian or non-Newtonian rheology, *J. Geophys. Res.*, 104(B6), 12,759–12,777, doi:10.1029/1999JB900110.
- Durham, W. B., O. Prieto-Ballesteros, D. L. Goldsby, and J. S. Kargel (2010), Rheological and thermal properties of icy materials, *Space Sci. Rev.*, 153(1-4), 273–298, doi:10.1007/s11214-009-9619-1.
- Gerrard, J. A. F., M. F. Perutz, and A. Roch (1952), Measurement of the velocity distribution along a vertical line through a glacier, *Proc. R. Soc. London A*, 213(1115), 546–558.
- Goodman, D. J., H. J. Frost, and M. F. Ashby (1981), The plasticity of polycrystalline ice, *Philos. Mag. A*, 43(3), 665–695, doi:10.1080/01418618108240401.
- Grasset, O., and E. M. Parmentier (1998), Thermal convection in a volumetrically heated, infinite Prandtl number fluid with strongly temperature-dependent viscosity: Implications for planetary thermal evolution, *J. Geophys. Res.*, 103(B8), 18,171–18,181, doi:10.1029/98JB01492.
- Howard, L. (1966), Convection at High Rayleigh Number, *Springer, Berlin Heidelberg*, pp. 1109–1115, doi:10.1007/978-3-662-29364-5-147.
- Husmann, H., C. Sotin, and J. Lunine (2007), 10.15—Interiors and evolution of icy satellites, in *Treatise on Geophysics*, pp. 509–539, Elsevier, Amsterdam, doi:10.1016/B978-0-44452748-6.00168-1.
- Jarvis, G. T., G. A. Glatzmaier, and V. I. Vangelov (1995), Effects of curvature, aspect ratio and plan form in two- and three-dimensional spherical models of thermal convection, *Geophys. Astrophys. Fluid Dyn.*, 79(1-4), 147–171, doi:10.1080/03091929508228995.
- Lewis, J. S. (1971), Satellites of outer planets—Their physical and chemical nature, *Icarus*, 15(2), 174–185, doi:10.1016/0019-1035(71)90072-8.
- Moresi, L. N., and V. S. Solomatov (1995), Numerical investigation of 2D convection with extremely large viscosity variations, *Phys. Fluids*, 7(9), 2154–2162, doi:10.1063/1.868465.
- O'Farrell, K. A., and J. P. Lowman (2010), Emulating the thermal structure of spherical shell convection in plane-layer geometry mantle convection models, *Phys. Earth Planet. Inter.*, 182(1-2), 73–84, doi:10.1016/j.pepi.2010.06.010.
- O'Farrell, K. A., J. P. Lowman, and H.-P. Bunge (2013), Comparison of spherical-shell and plane-layer mantle convection thermal structure in viscously stratified models with mixed-mode heating: Implications for the incorporation of temperature-dependent parameters, *Geophys. J. Int.*, 192(2), 456–472, doi:10.1093/gji/ggs053.
- Ratcliff, J. T., G. Schubert, and A. Zebib (1995), Three-dimensional variable viscosity convection of an infinite Prandtl Number Boussinesq fluid in a spherical shell, *Geophys. Res. Lett.*, 22(16), 2227–2230, doi:10.1029/95GL00784.
- Ratcliff, J. T., G. Schubert, and A. Zebib (1996), Effects of temperature-dependent viscosity on thermal convection in a spherical shell, *Physica D*, 97(13), 242–252, doi:10.1016/0167-2789(96)00150-9.
- Reese, C. C., V. S. Solomatov, J. R. Baumgardner, and W. S. Yang (1999), Stagnant lid convection in a spherical shell, *Phys. Earth Planet. Inter.*, 116(1-4), 1–7, doi:10.1016/S0031-9201(99)00115-6.
- Reese, C. C., V. S. Solomatov, and J. R. Baumgardner (2005), Scaling laws for time-dependent stagnant lid convection in a spherical shell, *Phys. Earth Planet. Inter.*, 149(3-4), 361–370, doi:10.1016/j.pepi.2004.11.004.
- Shahnas, M. H., J. P. Lowman, G. T. Jarvis, and H.-P. Bunge (2008), Convection in a spherical shell heated by an isothermal core and internal sources: Implications for the thermal state of planetary mantles, *Phys. Earth Planet. Inter.*, 168(1-2), 6–15, doi:10.1016/j.pepi.2008.04.007.
- Solomatov, V. S. (1995), Scaling of temperature-dependent and stress-dependent viscosity convection, *Phys. Fluids*, 7(2), 266–274, doi:10.1063/1.868624.
- Sotin, C., and S. Labrosse (1999), Three-dimensional thermal convection in an isoviscous, infinite Prandtl number fluid heated from within and from below: Applications to the transfer of heat through planetary mantles, *Phys. Earth Planet. Inter.*, 112, 171–190, doi:10.1016/S0031-9201(99)00004-7.
- Tackley, P. J. (2008), Modelling compressible mantle convection with large viscosity contrasts in a three-dimensional spherical shell using the Yin-Yang grid, *Phys. Earth Planet. Inter.*, 171(1-4), 7–18, doi:10.1016/j.pepi.2008.08.005.
- Tarantola, A., and B. Valette (1982), Generalized nonlinear inverse problems solved using the least squares criterion, *Rev. Geophys.*, 20(2), 219–232, doi:10.1029/RG020i002p00219.
- Tobie, G., G. Choblet, and C. Sotin (2003), Tidally heated convection: Constraints on Europa's ice shell thickness, *J. Geophys. Res.*, 108(E11), 5124, doi:10.1029/2003JE002099.
- Tobie, G., O. Grasset, J. I. Lunine, A. Mocquet, and C. Sotin (2005), Titan's internal structure inferred from a coupled thermal-orbital model, *Icarus*, 175(2), 496–502, doi:10.1016/j.icarus.2004.12.007.
- Travis, B., and P. Olson (1994), Convection with internal heat sources and thermal turbulence in the Earth's mantle, *Geophys. J. Int.*, 118(1), 1–19, doi:10.1111/j.1365-246X.1994.tb04671.x.
- Yoshida, M., and A. Kageyama (2004), Application of the Yin-Yang grid to a thermal convection of a Boussinesq fluid with infinite Prandtl number in a three-dimensional spherical shell, *Geophys. Res. Lett.*, 31, L12609, doi:10.1029/2004GL019970.